# Solar Potential Analysis Method Using Terrestrial Laser Scanning Point Clouds

Pengdi Huang, Ming Cheng, *Member, IEEE*, Yiping Chen, Dawei Zai, Cheng Wang, *Senior Member, IEEE*, and Jonathan Li, *Senior Member, IEEE*

*Abstract*—Analysis of sunlight or solar potential requires the data for a targeted scene to be authentic and accessible as much as possible. In this regard, the data for a real-world scene acquired by ground-based laser scanners are comprehensive and convenient, thus potentially meeting this requirement. To get an accurate result and offer an automatic solution for sunlight analysis, this paper proposes a solar potential analysis method that is run directly on 3-D ground laser scanning point clouds. Our method simulates natural illumination, sunlight hours, and solar radiation of the targeted scene for a specified period. This method first extracts the region of interest (ROI) to obtain targeted points. Then, we compute solar position as a virtual light source and propose a control method acting on the ROI to constraint deviation from the point light source. Finally, we adopt the generalized hidden point removal algorithm to cast shadow of obstruction on the ROI. Besides, experiments to validate the shading method results are carried out for three different periods. The quantitative results in the Xiamen case evaluated by the Hausdorff distance demonstrate the advantage and feasibility of our proposed method.

*Index Terms*—Generalized hidden point removal (GHPR) operator, shadow analysis, solar energy potential, terrestrial laser scanning (TLS), 3-D point clouds.

## I. INTRODUCTION

SOLAR radiation is affected by the shape and structure of a terrain, thereby presenting redistribution on a local scale. Because the distribution of solar radiation in a complex scene depends on the relationship among time, location, weather conditions, and casting shadows, an obstruction analysis is necessary [1]. In particular, in an urban scene, sunlight is often occluded by urban structures (e.g., buildings). Besides, since the daylighting of a solar device on a building is likely in self-occlusion (due to building's structures and auxiliaries), an elaborate analysis is also necessary. Therefore, implementation of spatial–temporal shadow analysis is helpful to estimating actual solar radiation.

In addition, using 3-D analysis, Helbich *et al.* [2] demonstrate that urban house price can be estimated more precisely by considering shadowing effects and solar radiation. Other 3-D analysis applications include how a terrain influences daylighting of crops for the optimization of crop planting [3], where the resolution of the simulation scale is down to plant leafs' size. Such evolving special models call for a scene restoring approach to implement a careful analysis. In general, obstruction analysis of the targeted scene is carried out through geographical information system (GIS) analysis of the input data. An ideal input data source should represent geometric structures in fine details and be readily obtainable. GIS analysis mainly uses shading methods (also called natural illumination simulation [4]) to analyze spatial relation between objects in the input data for GPS. In fact, the increasing demands on the special models mean that the topographic shading method is also playing a more and more important role in these models.

Since solar potential analysis relies on a compound method, its progress is advanced by the development of data acquisition and data-driven processing methods. As usual, raw input data will be processed as georeferenced models, e.g., the digital elevation model (DEM), or the 3-D model, for shadow analysis. For building objects, 3-D models can be derived from diverse data sources, but they rely on interactive operations [5], [6]. DEM effect depends on the accuracy of raw data. For instance, for macroscale analysis, images were used to make DEM for computing topographic shadows [7]. For a more complex terrain type, the resolution of adoptive DEM is 30 m in cooperating with topographic correction of satellite imagery [8]. In particular, 3-D point clouds acquired by a laser scanner record positions of scanned object surfaces. Airborne laser scanning (ALS) point clouds with horizontal resolution 1 m have been used to generate DEM for shadow analysis [9].

However, ALS point clouds are deficient in data integrity. Due to aerial perspective, building facades and objects under vegetation canopy (e.g., ground) are lost in data acquisition. Thus, ALS point clouds form an elevation layered structure with plenty of gaps, which hinders direct occlusion analysis in the raw point clouds. Besides, for solar potential analysis on a microscale, ALS data are limited by data accuracy. Loss of small architectural elements (e.g., balcony, windows, and roof tank) causes

P. Huang, M. Cheng, Y. Chen, D. Zai, and C. Wang are with the Fujian Key Laboratory of Sensing and Computing for Smart Cities, School of Information Science and Engineering, Xiamen University, Xiamen 361005, China (e-mail: alualu628628@163.com; chm99@xmu.edu.cn; ypchenhk@gmail.com; david102812@gmail.com; cwang@xmu.edu.cn).

J. Li is with the Fujian Key Laboratory of Sensing and Computing for Smart Cities, School of Information Science and Engineering, Xiamen University, Xiamen 361005, China, and also with the Department of Geography and Environmental Management, University of Waterloo, Waterloo, ON N2L 3G1, Canada (e-mail: junli@uwaterloo.ca).

the generated model of ALS data too simple to mimic reality. Facades close to each other in ALS point clouds can also cause errors [1]. Besides, some roof modeling methods produce unreliable results for modeling low-resolution ALS data and thus affect the final results [10]. In fact, large-scale data collection of ALS offers no advantage to a small project of solar energy potential evaluation, but the data are still rare and expensive to obtain nowadays [11]. Facing these problems, this paper prefers terrestrial laser scanning (TLS) and mobile laser scanning (MLS) point clouds. TLS and MLS point clouds are accurate and accessible and retain high-resolution geometric information for periodical monitoring and mapping of the environment (e.g., detection of changes) [12], [13]. From a ground perspective, a ground laser scanner obtains the spatial information of all overhead obstructions for the survey scene without any omission. In addition, the portability of a TLS device is appropriate for carrying out specific solar energy resources investigations. However, how to utilize the spatial information of high-resolution geometry in TLS point clouds to produce solar potential on a microscale has been lacking. In this paper, we present a new solar potential analysis method using TLS point clouds.

The contribution of this paper is presentation of a solar potential analysis method directly based on ground-based laser scanning point clouds without data distortion and *a priori* hypothesis of a scene. The main novelties are as follows. First, we propose a method considering solar position as a virtual point light source at a point cloud scene and adopting a generalized hidden point removal (GHPR) algorithm to cast shadow of the whole scene. Second, we propose a deviation control method in a point cloud scene to restrain deviation between different kinds of light sources. Third, we design a repeatable verification experiment and a result evaluation method to quantitatively analyze natural illumination simulation results.

The rest of this paper is organized as follows. A simple review on previous work of solar potential evaluation based on point clouds is presented in Section II. The methodology containing region-of-interest (ROI) extraction, solar positioning, natural illumination simulation, solar potential evaluation, and result evaluation method is detailed in Section III. Discussion of experimental data and results and conclusions are presented in Sections IV and V, respectively.

## II. RELATED WORK

Shading and solar potential assessment using laser scanning point clouds is driven by strong data demand. The work by related studies mainly concentrated on ALS point clouds, which represent the height of each urban component [14]. However, with the development of object segmentation in various scenes (e.g., urban [15], highway [16], and railway [17]), the ground laser scanners (e.g., TLS [18] and MLS [19]) were also involved in some of the related research works. The utilization mode of point cloud data can be classified into two kinds: the methods relying on modeling point clouds and the methods directly based on point clouds.

For the methods relying on modeling, in some studies, point cloud data are used to generate a digital surface model (DSM), and shadow volume computing will directly perform on the grids

of the DSM [20]–[22]. To ensure the quality of a solar radiation flux model, high resolution of the DSM is usually required, which can be gained through point interpolation of the raw data [23]. Other researchers used a model reconstruction method in point cloud data to achieve a finer structure of a city model (e.g., a polygon model [10] and a simple block model [24]), which requires *a priori* parameters referring to the modeled object (e.g., building and tree) [25]. Considering facade loss in the DSM, Catita *et al.* proposed a method fusing a DSM model and a building model [26]. However, due to the scene complexity of an urban environment, the way of modeling was almost always through interactive or semiautomatic methods, e.g., handling the well-known CityGML [27]. In this manner, the ALS point cloud data only offer an elevation reference for reconstruction [28]. Besides, there are still some flaws impairing the modeling of urban objects, e.g., individual tree automatic segmentation should be further improved for vegetation surface reconstruction [29].

In fact, a finer level of detail of a city model may bring negligible improvement of shadow effects but higher costs of acquisition and processing, depending on the configuration of the modeled object [30]. Therefore, in recent years, finding a solution directly based on raw point clouds has attracted more attention. For example, Jochem *et al.* [31] detected roof plane points first and, then, implemented an area partition method for each detected point to judge shade point. Considering a detected point as a center, the area partition method was to subdivide the horizontal plane into fan sections with a given azimuth interval. Then, the section containing current solar azimuth will be determined, and the highest point of this section would be found to judge whether it was higher than the solar elevation angle. This model was also applied into MLS data [19]. Lukač also proposed a brute force method based on the height value, which found the grids lower than the line from solar position to the query gird as being in shadow [32]. This method was also sped up by a graphics-processing-unit-based method [33] and embedded into a precise photovoltaic potential assessment model [34].

To sum up, the existing methods mainly run on ALS point clouds, and some of the derived 2.5-D shading methods are powerless to utilize 3-D data [35]. Besides, in the methods directly based on point clouds, the main principle is also based on a simple idea that a pixel (or raster, grid) is in shadow if a higher point (indicating the vertical facade without hole) lies upon the ray between sun and the pixel. The high-resolution geometry, shape, and type of obstruction have no regard for processing. In this paper, for TLS and MLS point clouds, we propose a method that focuses on reserving the details (local level) of shadow effects in the scene, so as to mimic a complex environment and meet various application purposes.

## III. METHOD

We propose a solar illumination simulation method that is directly based on 3-D laser scanning point clouds. As shown in Fig. 1, the process of this method includes four steps: ROI extraction, solar positioning, illumination calculation, and solar radiation computing. In ROI extraction, we obtain targeted
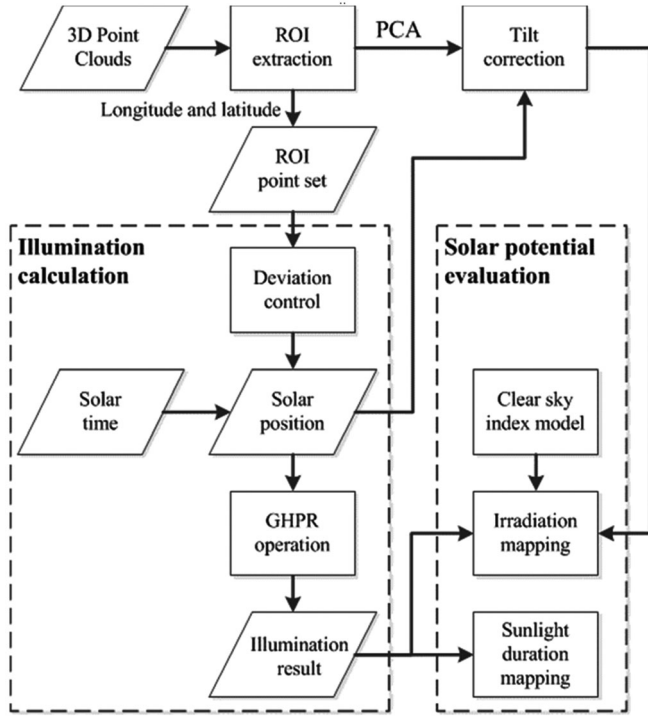
Fig. 1.   Framework of the proposed method.



Fig. 2.   Results of ROI extraction of two point cloud scenes. (a) and (c) Raw point clouds. (b) and (d) Extraction points indicated with green color.

point set of the survey area. In solar positioning, for an ROI, a geographic system is embedded into the method to prepare for solar position computing. In illumination calculation, an error control method is first proposed to control the deviation of different light sources, and the GHPR algorithm is then adopted to cast shadow in an ROI. In solar potential evaluation, we show two applications, i.e., sunlight duration and solar radiation computing for actual production.

### A. ROI Extraction

The investigation area of solar potential estimation refers to a large open area where a solar collection facility would be installed, e.g., roof, ground, balcony, or facade. In practice, an investigation area in point clouds could be selected by an interactive operation, but we devote to offer an automatic approach. The purpose of this paper is to present a method that determines where a small-scale solar energy facility (e.g., domestic solar water heaters) would be best located. Therefore, we define the ROI as the points belonging to the investigation area in a point cloud scene, i.e., roof points in our cases.

Before ROI extraction, point reduction is suggested at the beginning of this method, because high point density is unnecessary and cumbersome for illumination computing. Thus, we have adopted the classical voxel grid filter, which uses a voxel's center of gravity to replace points within the voxel. After point reduction, the mean distance of two neighboring points is approximate to the given voxel side length of filtering. We, thus, denote a given voxel side length as sampling interval $\rho$ in this paper.
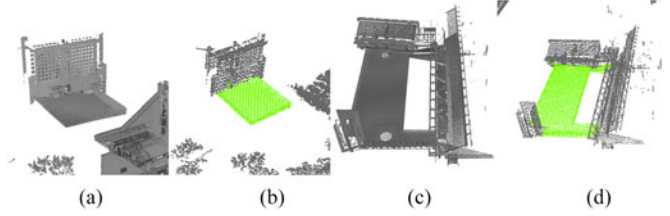
To extract ROI, we adopted the upward growth ground point extraction method [36], [37]. Due to auxiliaries and unevenness of an ROI, such as a roof insulation layer, covering tiles, or a roof garden, the roof should not be considered as a simple plane. This voxel method frees from the restriction of plane assumption and extracts potential ground points under a specific height. Thus, the parameter adjustment from ground to roof point extraction is given an elevation value that is higher than the targeted roof (or alternatively 3 m higher than the scanner position if such a position is available). Then, a Euclidean clustering is carried out to cluster ground points into a series of objects. From there onwards, we compute density of each object in raw point clouds and choose the highest one. The reason is that, in the data collection link, the laser scanner is required to be placed at the targeted area to achieve a complete scene. Therefore, the ROI is nearer to the scanner, shown as dense points than background. In short, significant density value of the ROI is a stable clue for distinguishing the ROI from background. Fig. 2 shows ROI extraction results with $\rho = 0.5$ m, where green points are the extracted points.

### B. Calculating Solar Position in 3-D Point Clouds

In our method, the sun will be considered as the light source of a point cloud scene, and positioning light source is a necessary step for our system. To a point $p$, first, we transform its coordinate (WGS84 in this paper) to longitude and latitude $[L_p, B_p]^T$, expressed as $p = [L_p, B_p, H_p]^T$. Some methods were proposed to (see [38]) compute solar azimuth and altitude angle, but we use a simple method in [39] that requires only existing longitude, latitude, and solar time. Solar azimuth and altitude indicates the solar orientation. Different from the other methods, we generate a virtual point as the light source in a point cloud scene, which requires the solar distance. Then, based on solar azimuth angle $\psi_A$, solar elevation angle $\psi_E$, and solar distance $D_s$, the solar position at point $p$ is expressed as s, where $s = [L_p + T_l(s_y), B_p - T_l(s_x), H_p + s_z]^T$, $T_l$ is the transformation from length to longitude–latitude. $s$ is computed as follows:

$$s_x = D_s \sin(\pi/2 - \psi_E) \cos(\psi_A)$$
$$s_y = D_s \sin(\pi/2 - \psi_E) \sin(\psi_A)$$
$$s_z = D_s \cos(\pi/2 - \psi_E). \tag{1}$$

Then, $s$ and $p$ are converted back to WGS84 coordinates. Thus, we have $\|p - s\| = D_s$, where $\| \cdot \|$ is a vector norm. In
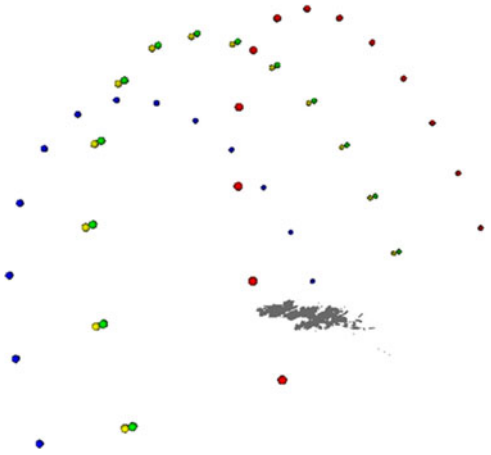
Fig. 3. Solar positions of a scene on four days in 2020: green dots show the position on March 20, red dots on June 21, yellow dots on September 22, and blue dots on December 21.



Fig. 4. Graphic analysis of point light source and directional light in arbitrary point in point clouds.

practice, $D_s \to \infty$, as the distance between the sun and the earth is far greater than the length of the scene. However, for the sun position, $D_s$ should be a reasonable value or the scene would be collapsed to a point from a distant observation. Fig. 3 shows, with a 600-m $D_s$, the solar positions of spring equinox, summer solstice, autumn equinox, and winter solstice in 2020, which are based on the center of the point cloud scene, respectively. The changing of the solar position forms apparent motion of the sun in the point cloud scene.

Since an ROI often includes a tilted surface, a correction considering the tilt factor should be executed after solar positioning. In point clouds, the normal vector of a point neighboring surface is achieved by the principal-component-analysis-based approach. The unit normal vector $v_n$ is estimated by the eigenvector corresponding to the smallest eigenvalue of covariance matrix $M$ after matrix decomposition. The covariance matrix $M$ is shown as

$$M = \frac{1}{u} \sum_{i=1}^{u} (q_i - \bar{q})(q_i - \bar{q})^T \qquad (2)$$

where $q_i$ is the neighboring points of $p$, $\bar{q}$ is the center of the neighboring point set, and $u$ is the cardinality of the neighboring point set. Besides, we have the incidence vector of a point as $s - p$. The correction factor $\tau$ is computed by cosine of the angle between incidence vector and the normal vector of local surface as follows:

$$\tau = (s - p) \cdot v_n / D_s \qquad (3)$$

where "·" represents dot product. Thus, to prepare for illumination calculation, the normal vector of each point in the ROI will be computed following ROI extraction.

### C. Illumination Calculation

In the illumination calculation link, we propose adopting the GHPR algorithm [40] for shadow casting. However, the GHPR algorithm is a point-light-source-based algorithm, whereas sunbeam, due to the long distance between the earth and the sun,
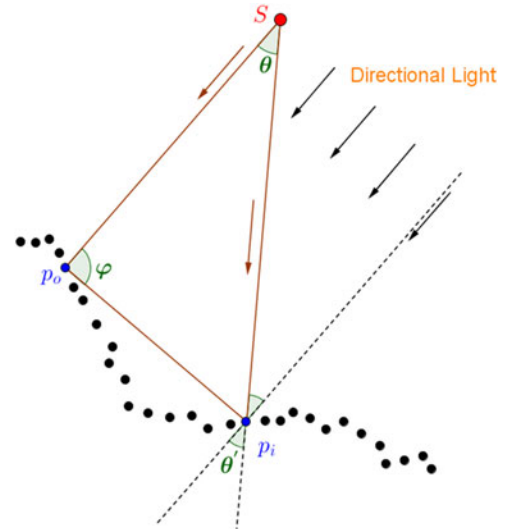
is usually considered as parallel light. With our method, a virtual point light source is set at the solar position, and it emits virtual light along the radioactive route. Other than being shone by the actual sunlight from the same direction, each point in the point clouds is shone by a ray from a slightly different direction. This situation causes deviation in the position of the shadow. Accordingly, we propose a deviation management method for the simulated ray (coming from the point light source) and the actual sunlight (coming from the directional light source) in the point cloud scene.
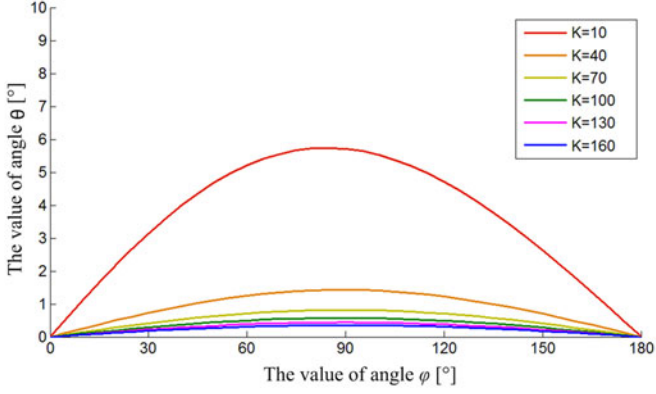
*1) Deviation Analysis:* For a reference point $p_o$ and its solar position $s$, given any point $p_i$ out of a straight line segment with endpoints $p_o$ and $s$, a plane can be constructed as shown in Fig. 4. In this plane, to point $p_i$, $\theta$ is the deviating angle between the parallel ray and the ray emitted from $s$, and we have

$$\frac{\|p_o - p_i\|}{\sin\theta} = \frac{\|p_o - s\|}{\sin(\pi - \varphi - \theta)} \qquad (4)$$

where $\varphi$ is the angle between the line segment with endpoints $p_o$ and $s$ and the line segment with endpoints $p_o$ and $p_i$. Due to $\|p_o - s\| = D_s$, for $\theta$, (4) can be derived as

$$\theta = \cot^{-1}\left(\frac{K - \cos\varphi}{\sin\varphi}\right), \quad K = \frac{D_s}{\|p_o - p_i\|} \qquad (5)$$

where $K$ and $\varphi$ are distance and angle variable of $\theta$ after simplification formula, respectively. As seen, $K$ is the ratio of $D_s$ to the distance between point $p_o$ and $p_i$, which is used to measure whether the solar distance is far enough relative to a surface distance. The offset of casting shadow is dependent on $\theta'$, and $\theta' = \theta$. In (5), $\theta$ is influenced by $\varphi$ and $K$. Thus, reducing the value of $\theta$ will reduce probable deviation. However, the value of $\varphi$ varies according to the position relationship between $p_o$ and any point $p_i$, even though $0 < \varphi < \pi$. In particular, parameter $K$ is easier to be controlled. Increasing $D_s$ and decreasing $\|p_o - p_i\|$ both can reduce $\theta$. As shown in Fig. 5, the vertical and horizontal axes indicate respective values of $\theta$ and $\varphi$ in degree

Fig. 5.  Relationships among variables $\theta$, $\varphi$, and $K$.



Fig. 6.  Computing base points and partitioning ROI of one point cloud scene with 600-m solar distance and different $\theta'$ values: (a) $\theta' = 1.0$; (b) $\theta' = 2.0$; (c) $\theta' = 3.0$.

measure [°]. With the same $K$ value, and due to $K \gg \cos\varphi$, $\theta$ becomes largest if $\varphi \to \pi/2$. With $K$ increasing, $\theta$ approaches to zero, indicating that the deviation is under control.

To sum up, one solar position for an entire scene is insufficient. However, computing GHPR once for each point is redundancy and unduly burdensome. Besides, it is difficult to place solar position in a great distance, because $D_s \to \infty$ will make the scene become tiny relative to the solar position. Therefore, to control deviation and number of operations, we proposed a method by limiting the value of $\|p_o - p_i\|$, i.e., restricting the action range of solar position $s$ of point $p_o$.

*2) Deviation Control:* Assuming the point set of an ROI as $\tilde{P}$, $\tilde{p}_i \in \tilde{P}$, our proposed deviation control method gives a certain number of solar positions in the point cloud scene as a set, $S$, where $S = \{s_k | k = 1, 2, \ldots, m\}$, and obtains the corresponding cell (small region) of the ROI in charge of each solar position $s_k$ in illumination calculation as $R_k$, where $\tilde{P} = \bigcup_{k \in [1,m]} R_k$.

The first step is setting up an acceptable deviation to obtain the partition size for partitioning ROI. Partition size $d_p$ is determined by aforementioned deviation angle $\theta'$ and solar distance $D_s$ as

$$d_p = \frac{D_s}{\tan\left(\pi/2 - \theta'\right)}. \tag{6}$$

Setting the deviation value for $\theta'$ is equivalent to controlling the value of $d_p$. In this paper, 1° of $\theta'$ is considered to be acceptable. This is because, with this value, for an obstruction within 100-m distance, the maximum shadow deviation caused by the vertical incident ray is less than 1.75 m, which should be acceptable for analyzing the interference by an adjacent facility. However, for an investigation area near a super high-rise building, we would suggest using a smaller $\theta'$ value. The second step is partitioning ROI. We define one kind of points as base point, $o_k$, which is used as reference point to compute solar position $s_k$ and to help partitioning ROI as $R_k$, $R_k = \{\tilde{p}_i \in \tilde{P} | \|\tilde{p}_i - o_k\| \le \|\tilde{p}_i - o_n\|, \ n \in [1, m] \text{ and } n \neq k\}$. Therefore, to ensure that each point $\tilde{p}_i$ satisfies the condition $\|\tilde{p}_i - o_k\| \le d_p$, the number of $o_k$ (denoted as $m$) should be computed first to ensure their action range covering the whole ROI point set $\tilde{P}$. An ideal result for base point selection asks
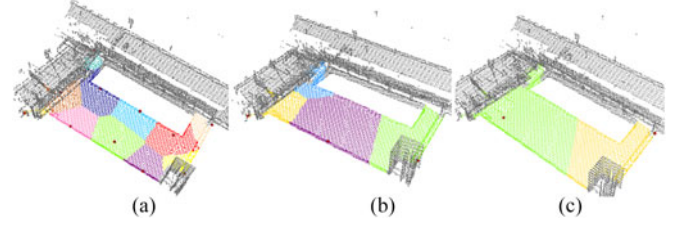
for the smallest value of $m$ leading to $\tilde{P} = \bigcup_{k=0}^{m} R_k$, which is a typical set cover problem.

Thus, we propose using the greedy permutation method, which is used as the sampling algorithm [41], to fast select base points for an approximate result. This algorithm randomly selects a point in the ROI as initial base point $o_1$ and constructs a sequence $O = \{o_1\}$. Then, the farthest point in the ROI to sequence $O$ is successively added to $O$ as $O = \{o_1, o_k, \ldots, o_m\}$, until there is not a point $\tilde{p}_j, \tilde{p}_j \in \tilde{P}$, satisfying $\min_{k \in [1,m]} \|o_k - \tilde{p}_j\| \ge d_p$.

Finally, each point $\tilde{p}_i$ is allocated to the nearest neighboring base point as a set $R_k$, which is equivalent to computing the Voronoi diagram in base point set $O$ across $\tilde{P}$ [42]. In addition, solar position $s_k$ of each base point $o_k$ is also computed for the points belonging to the corresponding $R_k$. As shown in Fig. 6, the ROI points are divided into a series of cell in different colors based on the base point (red ball). The probable deviation of each point in the ROI is under $d_p$.

*3) Shadow Casting:* We proposed using the GHPR algorithm for shadow casting in raw point clouds without any surface modeling. The GHPR algorithm is developed for various purposes, e.g., point reduction [43] and viewpoint selection [44], both of which emphasize on vision understanding of point clouds. This paper mainly utilizes shadow casting ability of GHPR in a large-scale point cloud scene. Given a solar position $s$ and a 3-D point set of the survey scene $P$, $P = \{p_i | i = 1, 2, \ldots, w\}$, where $w$ is the cardinality of the point set, the GHPR is first implemented by a geometric transformation of $T_f$ to $p_i$ as

$$\breve{p}_i = T_f(p_i, s) = \begin{cases} s + \dfrac{p_i - s}{\|p_i - s\|} f_k(p_i, s), & p_i \neq s \\ p_i, & p_i = s \end{cases} \tag{7}$$

where $\breve{p}_i$ is the $p_i$ after transformation, and $f_k(p_i, s)$ is the kernel function of the transformation. In this paper, we use the linear kernel [45]. For the given $s$ and $P$, we have a radius of spherical flipping $R$, $R = \max_{p_i \in P} \|p_i - s\|$; thus, the linear kernel function is computed by point $p_i$ and its solar position $s$ as

$$f_k(p_i, s) = 2\gamma R - \|p_i - s\| \tag{8}$$

where $\gamma$ is the distance adjusting parameter, $\gamma \ge 1$. In addition, since $\gamma$ is often large, we use parameter $\alpha$, where

$\alpha = \log(\gamma)$. Then, a convex hull computation is carried out for $\breve{P} \cup \{s\}$, where $\breve{P}$ is the transformed point set, and $\breve{P} = \{T_f(p_i, s) | p_i \in P\}$. The shadow point set $W$ consists of the points within the convex hull and will be labeled after convex hull computation.

Thus, to each solar position $s_k$, we compute a $W_k$ for the corresponding point set $R_k$. The shadow casting result of the entire ROI $C$ is computed as follows:

$$C = \bigcup_{k \in [1,m]} \left( W_k \bigcap_{k \in [1,m]} R_k \right) \quad (9)$$

where $m$ is the cardinality of point set $S$. Thus, the illumination condition of any point can be presented as in shadow (value 0) or in sunlit area (value 1) by a binary function:

$$f_b(p_i, C) = \begin{cases} 1, & \{p_i\} \cap C = \varnothing \\ 0, & \{p_i\} \cap C \neq \varnothing \end{cases} \quad (10)$$

where $f_b$ is the binary function. In particular, in (8), $f_k(p_i, s) \to \infty$ if parameter $\alpha \to \infty$ ($\gamma \to \infty$) or $D_s \to \infty$ ($\max_{p_i \in P} \|p_i - s\| \geq D_s$), which would lead to all points visible as $W = \varnothing$. For good performance, appropriate values of parameters $\alpha$ and $D_s$ should be determined before implementing illumination simulation. Besides, because raw point clouds are sampled with a fixed value at the beginning, sampling interval should be also considered for performance. Therefore, we present a parameter analysis experiment with different sampling intervals. Note that the parameter analysis result is universally applicable, not requiring scene assumption.

### D. Application of Solar Potential Evaluation

Sunlight duration is one important index to measure whether natural lighting of buildings [46] and/or city layout [47] are reasonable. We define $N(p_i)$ as sunlight duration of a point $p_i$, which can be calculated as

$$N(p_i) = \sum_{t=t_{sr}}^{t_{ss}} f_b(p_i, C_t) \quad (11)$$

where $t_{sr}$ and $t_{ss}$ are sunrise and sunset times, respectively. $t_{sr}$ and $t_{ss}$ are easily determined by solar elevation angle $\psi_E$, and an additional condition for $t_{sr}$ and $t_{ss}$ is that solar elevation $H_s$ exceeds the elevation value of computed point $p_i$ as $H_p$, $H_s > H_p$.

The second application is solar radiation evaluation. With data including geographic coordination information, a clear sky model can be directly performed without considering occlusion [48]. For a point $p_i$, the global radiation $E_g$ [kWh/m$^2$] is estimated by solar direct radiation $E_s$ [kWh/m$^2$] and solar diffuse radiation $E_d$ [kWh/m$^2$] as $E_g(p_i) = E_s(p_i) + E_d(p_i)$. After considering the occlusion factor, direct irradiation of any point $p_i$ is rewritten as

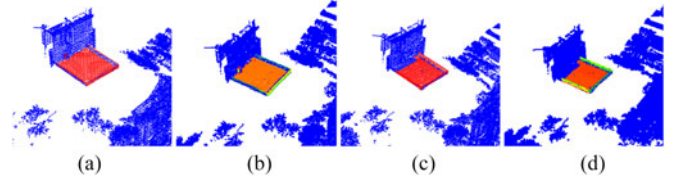$$E_s(p_i) = \sum_{t=t_1}^{t_2} I_s(t) f_b(p_i, C_t) \quad (12)$$



Fig. 7. Solar direct radiation [(a) and (c)] without and [(b) and (d)] with tilt correction of a point cloud scene: (a) and (b) at 15:00, June 20; (c) and (d) at 12:00, September 23.

where $I_s(t)$ is the transient solar direct radiation on an ideal horizontal plane, which depends on the standard weather condition of the point cloud scene location and can be computed in [49] by the given longitude and latitude of the scene. $E_s$ is the direct radiation of a full day if $t_1 = t_{sr}$ and $t_2 = t_{ss}$. Considering surface slope, direct radiation can be computed by the stored correction factor $\tau$ as

$$E_s(p_i) = \sum_{t=t_1}^{t_2} I_s(t) f_b(p_i, C_t) \tau_{s_t, p_i} \quad (13)$$

where $\tau_{s_t, p_i}$ is the correction factor in regard to the solar position of a specific time at $s_t$ and $p_i$. Thus, through accumulated calculation, solar radiation of any period can be obtained in raw point clouds. One should note that the point density of data is usually less than 1 m$^2$; thus, actual irradiation of a point is equal to the point density of each square multiplying the calculated radiation. Fig. 7 shows that all nonshaded points without tilt correction are consistent in the direct irradiation result, but with tilt correction, they are sensitive to the solar position, as represented by color change between green (lowest) and red (highest).

### E. Evaluation Method

Result validation is still a challenge in developing solar potential models [1]. In fact, empirical analysis as a compromise was usually used to produce a rough judgment of the shadow casting results. Therefore, in this paper, we propose an evaluation method using the Hausdorff distance to obtain the quantitative accuracy of the computed results. Given two nonempty 3-D point sets $G$ and $B$ in the Euclidean space, the Hausdorff distance measures the Euclidean distance between each other. The Hausdorff distance is expressed as follows:

$$d_H(G, B) = \max \left\{ \sup_{g \in G} \inf_{b \in B} d(g, b), \sup_{b \in B} \inf_{g \in G} d(g, b) \right\} \quad (14)$$

where $d(g, b) = \|g - b\|$. The point set $G$ is defined as the ground truth point set of raw point clouds. The ground truth point set is formed by the actual boundary points between shaded and sunlit areas that are acquired by manually marking points on raw point data. The point set $B$ is formed by the boundary points of simulated shadow effects. Thus, in this paper, the Hausdorff distance measures the maximum distortion from calculated illumination distribution to actual illumination distribution, indicating the maximum offset we have to face.

For validation experiment, in the shaded area of the actual scanning scene, several targets will be placed orderly and

Fig. 8. Experimental dataset: image on the left showing the geographical position of survey scenes; image on the right an illustration of data collection procedure (the red box shows the scanning point clouds, the green box the targets placement in scene, and the orange box the same targets scanned into point clouds).



Fig. 9. Noise analysis by variation of parameter $\alpha$ and sampling interval $\rho$.

linearly on the boundary of the shadow at proper intervals. Meanwhile, the time of placement will be recorded. After data collection, the points belong to targets will be manually extracted as the ground truth set $G$. Besides, the boundary points of calculated shadow effects are also manually extracted (without omission from the results) as boundary point set $B$. This validation experiment must be executed under sunny weather condition.

Assuming a point cloud after sampling with a sampling interval $\rho$, we at least have $d_H(G, B) = n\rho$ if the casting shadow has an offset with $n$ point long. Besides, the $d_H(G, B)$ is also influenced by the distance of two adjacent targets. Compared to interval placement of the targets, the boundary points of the result are extracted without intervals. Thus, for each $g_i$ and its neighboring target $g_j$, it holds that $d_H(G, B) \geq \frac{1}{2}\max_{i \in [1,N]} \|g_i - g_j\| - \frac{1}{2}\rho$, where $j = \arg\min_{n \in [1,N]} \|g_i - g_n\|$, and $i \neq n$, and $N$ is the cardinality of set $G$. Thus, we have the limits of the measured result as $\frac{1}{2}\max_{i \in [1,N]} \|g_i - g_j\| - \frac{1}{2}\rho \leq d_H(G, B) < \infty$.

## IV. RESULTS AND DISCUSSION

### A. System and Data

There are three experimental datasets (Data I, II, and III), containing two complete rooftop scenes located in Haiyun campus of Xiamen University (N 24°25′59″, E 118°06′3″), Xiamen, China, as shown on the left-hand side in Fig. 8. The equipment we used is a RIGEL VZ-1000, a terrestrial laser scanner with a 1400-m scanning range. To ensure the integrity of the scanning results, we adopted a two-station scanning mode and a manual registration method. In fact, the above operation could be automated by using a laser scanner equipped with the GNSS device.

Data I and Data III were acquired at the rooftop of a teaching building on November 18, 2015, and May 12, 2016 at 09:29 (Beijing time) and 16:55 (Beijing time), respectively. In the morning of the November survey day, the east wall of the building cast a shadow on the scene (see the low right of Fig. 8). In the afternoon of the May survey day, a building directly to the west of the teaching building cast a shadow on the scene. Data II was acquired from the rooftop of the administrative
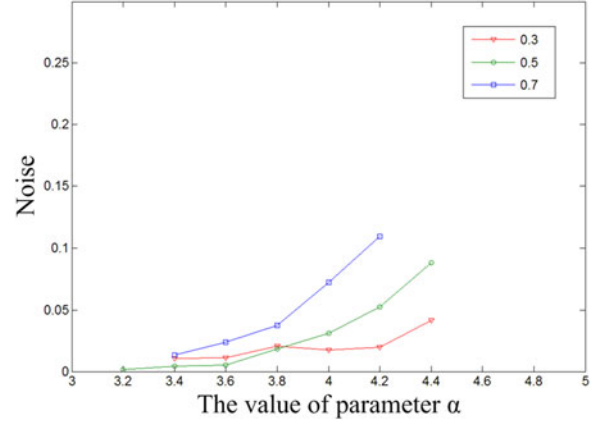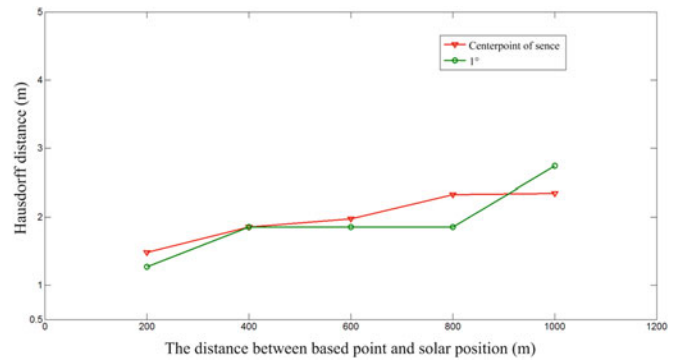

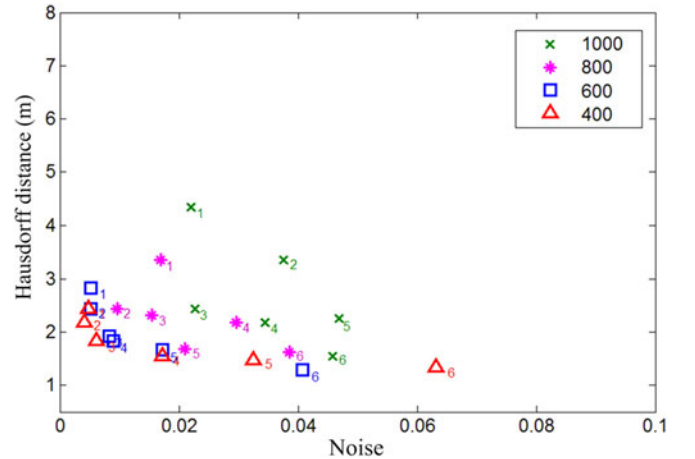
Fig. 10. Accuracy analysis by solar distance variation.



Fig. 11. Accuracy and noise analysis to find the optimal parameters, i.e., solar distance and parameter $\alpha$.

building (adjacent to the teaching building) on November 18, 2015, at 10:25 (Beijing time), at which time, a pavilion to the southeast of the rooftop cast a shadow on the scene. To validate results, before scanning, a series of yellow balls were accurately placed at the border of the shaded and sunlit areas as targets (as red circles in Fig. 8). The time was also recorded immediately upon the placement of the targets. The datasets
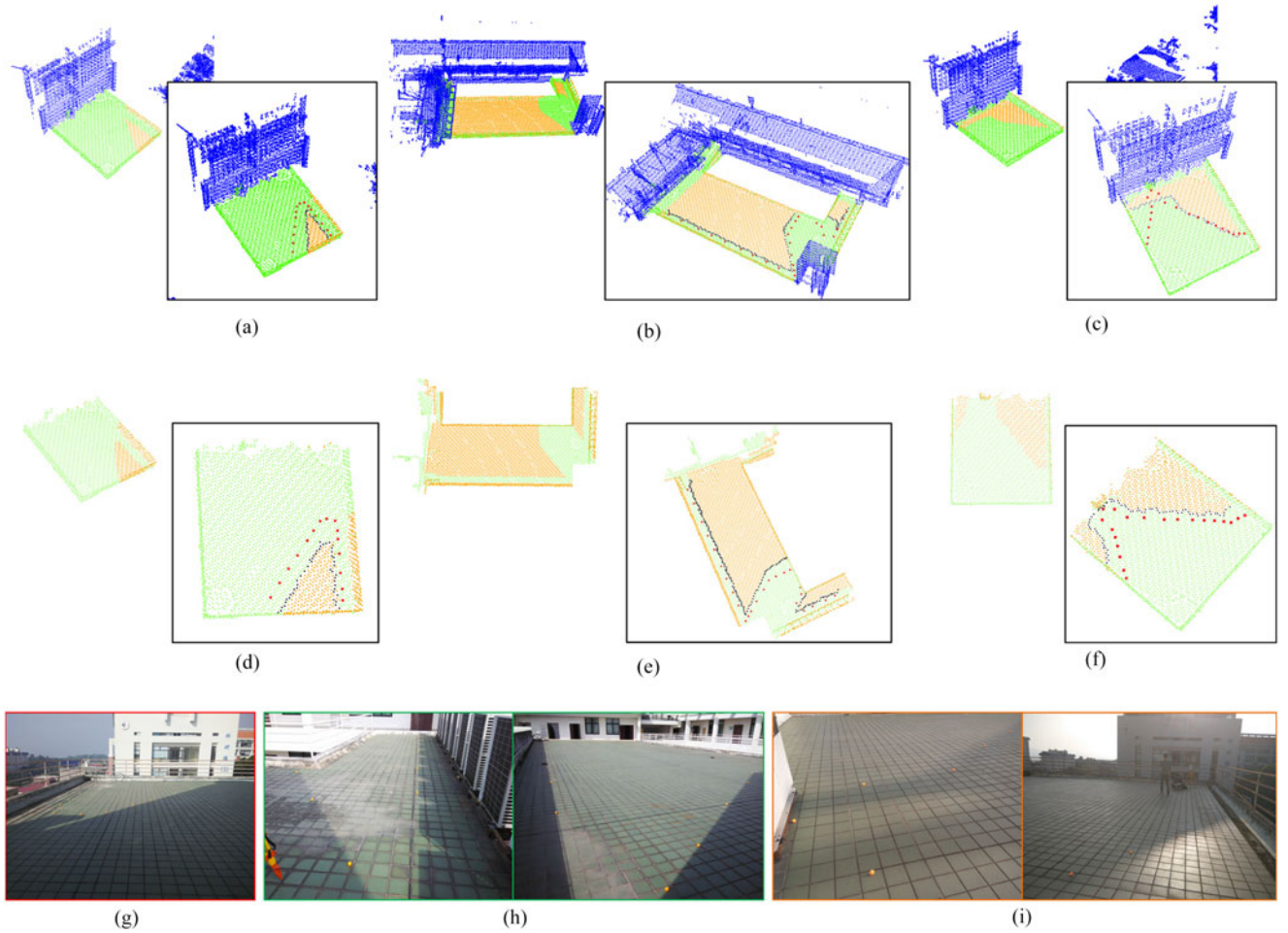
Fig. 12. Comparative results of three point clouds datasets. (a)–(c) Results of Jochem's method. (d)–(f) Results of our proposed method. (g)–(i) Ground truth of datasets.

(Data I, II, and III) are all GPS-ready 3-D point clouds. To obtain the ground truth, the positions of the targets (red circles) were manually confirmed and extracted from raw point clouds (see red box) as a ground truth point set. The experimental procedures were all coded in C++ and run on a personal computer configured with an Intel(R) Core(TM) i5-3470 CPU 3.2 GHz and a RAM 16.0 GB.

### B. Results

*1) Parameter Analysis:* To evaluate the results, we first need to define two concepts: noise and accuracy. In the results, there exists a noise phenomenon, namely, some shaded points are present in a sunlit area or some sunlit points are present in a shaded area, which are caused from points overlapping or junction between two facades. Therefore, the noise is computed as the percentage of the false point number in the total ROI point number. Noise suppression can improve the quality of details and makes the result smoother. The accuracy is defined as the degree of approximation between the simulated results and the actual illumination, which has previously been given a detailed introduction in the paper. Thus, in our proposed method, the

parameter that has the best performance would minimize noise and maximize accuracy, comprehensively.

First, we analyze the noise variation caused by different values of the parameter $\alpha$ and the sampling interval $\rho$. The false points will be manually labeled to compute the noise value. As shown in Fig. 9, the vertical and horizontal axes indicate the noise and parameter $\alpha$ value, respectively. Three colors correspond to three sampling interval of $\rho$. As seen, three curves are overall upwardly, which means that the noise value becomes greater as $\alpha$ becomes greater. The reason is that a greater $\alpha$ makes the boundary of shadow broader in the results and the corner structure thinner. However, the casting shadow shrinks when using a low $\alpha$, which reduces the accuracy of our method. Therefore, description of a noise and accuracy balancing experiment is added in the following section of this paper. Besides, the greater $\rho$, the earlier the curves rise. Hence, a small value of $\alpha$ ($\alpha < 4.0$) is appropriate to point cloud with a low sampling interval ($\rho \leq 0.5$).

Fig. 10 shows the comparative results in Data I. Red and green curves are that using center point of the ROI and based points with 1° deviation angle control, respectively. As previously said, $D_s$ and $\theta'$ both influence the accuracy of the results. The

TABLE I
EVALUATION RESULTS OF EXPERIMENTAL DATASETS USING
THE HAUSDORFF DISTANCE (M)

| Methods | Datasets | | | |
| --- | --- | --- | --- | --- |
| | Data I | Data II | Data III | Average |
| Jochem's method | 2.82233 | 2.43578 | 5.51119 | 3.58977 |
| Our method | 2.46228 | 2.18204 | 2.67861 | 2.44098 |



Fig. 13. Influence of built environment. (a) and (b) Tilt-out girder of building and its interference on results of a height-based method. (c) Illustration of radiation division.

vertical axis and horizontal axis represent the value of accuracy (Hausdorff distance $d_H(G, B)$) and solar distance $D_s$, respectively. As seen, the results with angle constraints have better performance from 200- to 800-m $D_s$. In particular, the accuracy of the results with 1000-m $D_s$ is mainly influenced by the edge error of GHPR, because the position difference between center point and based point is insignificant when compared with the larger $D_s$. Under the deviation control, the accuracy of the results remains within 2 m, meeting the practical needs of illumination estimation.

Fig. 11 shows the variation of noise and accuracy influenced by solar distance $D_s$ and parameter $\alpha$ ($\rho = 0.5$). The four colored signs correspond to samples with four different $D_s$. The subscript serial number of a sign from 1 to 6 represents the value of $\alpha$ from 3.4 to 4.4 with an interval 0.2. Besides, we give 1.0% of noise the same weight as 1 m of accuracy for the system. Therefore, as shown in Fig. 11, the test sample closer to the origin of coordinates has a better performance. Under the same Hausdorff distance, the noise value increases if $D_s$ becomes larger, which can be explained as simple as that the observation tend to be rough from a distant solar perspective. From the above, we use $\alpha = 3.8$ and $D_s = 600$ m for further application research. Note that under a specific sampling interval, the parameters of our method only need to be investigated once to meet the requirement of any future engineering.

*2) Comparative Experiments:* The solar illumination calculation of the visualization results of the three datasets are shown in Fig. 12. As shown, the blue points are background points, which are out of the ROI. The bright orange and green points are the points in the sunlit and shaded areas, respectively. Fig. 12(g)–(i) represents the ground truth of the experimental datasets. As we can see, the yellow ball targets are placed correctly on the boundary of the shadow in the actual scanning scene, corresponding to red points shown in the computed results. The boundary points of the casting shadow are manually labeled as black points in the results and extracted for further quantitative analysis. Fig. 12(a)–(c) represents the illumination results of Jochem's method [19], [31]. Jochem's method uses sector region segmentation and elevation judgment method to analyze sun shading in raw point clouds, and its procedure is detailed in Section II. This type of elevation-based method assumes that each scan point is on a smooth vertical facade without any hole. The parameters of Jochem's method we used are consistent with the value set in [50]. As shown, this method has good performance when the building has a simple structure. Fig. 13(a) and (b) shows that the protruding parts (red arrow)
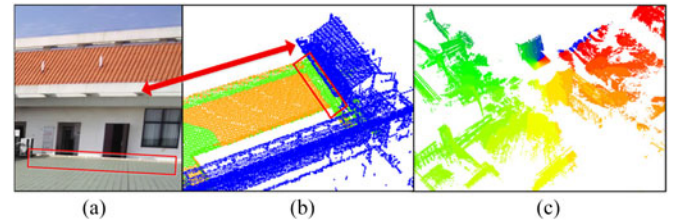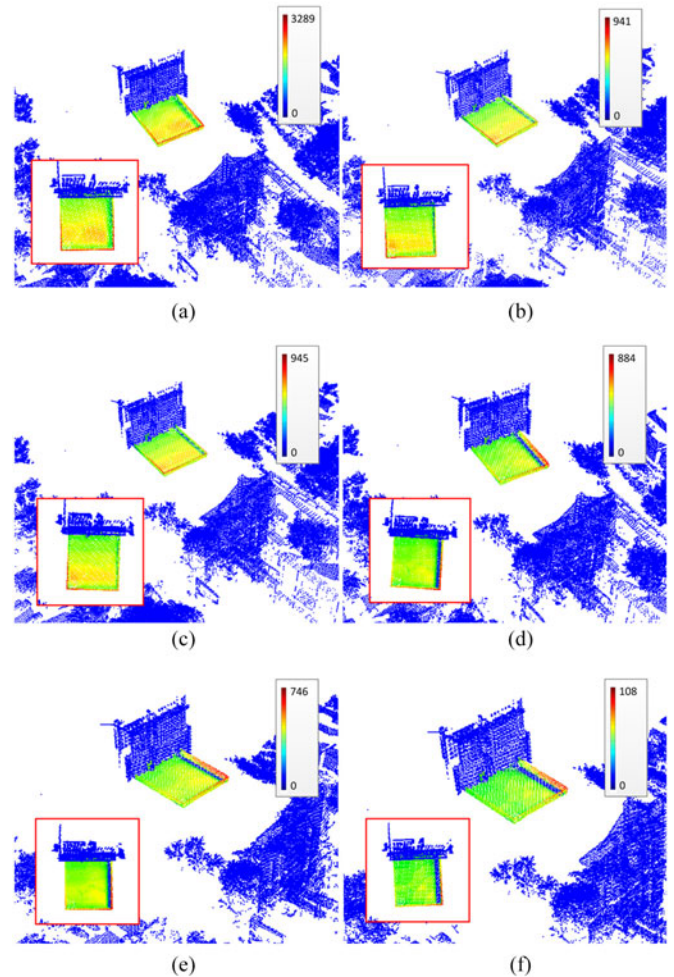


Fig. 14. Spatial distribution of sunlight durations of a full year and four seasons in Data I. (a) full year result; (b), (c), and (d) spring, summer, and autumn, respectively; (e) and (f) winter.

of the building can bring a challenge to this algorithm. Besides, the radiation form of the region segmentation approach in the algorithm suffers height value interference from distant objects [shown in Fig. 13(c)]. Fig. 12(d)–(f) shows the computed illumination result by our proposed method; the points not belonging to the ROI are removed from point clouds so as to give more intuitive showing. In our results, shadows are all in correct positions, as our method does not require any assumption of the investigated subject and does not exclude complicated structures of a building that are difficult to model. The influencing
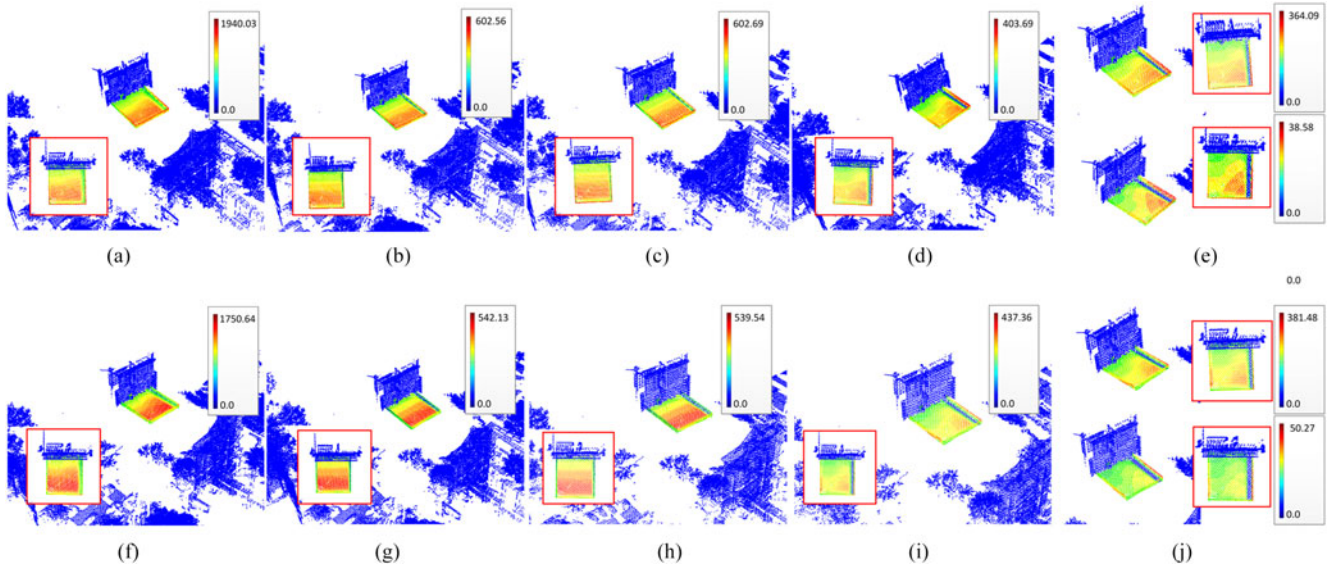
Fig. 15. Global irradiation in kWh/m$^2$ on one rooftop. (a)–(e) Annual sum, spring, summer, autumn, winter radiation of global irradiation without considering slope. (f)–(j) Annual sum, spring, summer, autumn, winter irradiation of global radiation with considering slope.

sources of illumination, e.g., handrails, girders, vegetation, and facades from a nearby building, are all considered for calculation. However, within the allowed error range, there are still some offsets on the casting shadow. Selecting a more appropriate $\alpha$ and a tighter $\theta'$ can further improve the accuracy of our results.

The quantitative results of the two methods are presented in Table I. As can be seen, evaluating by the Hausdorff distance, the average values of our method and Jochem's method are about 2.44 and 3.59 m, respectively. Because the Hausdorff distance is used to measure the maximum offset distance between casting and actual shadow, our proposed method is likely to maintain shape of the shadow edge. As an illustration of Data I, the running times of Jochem's method and our method are 3.78 and 0.45 min, respectively. In one illumination calculation, our method keeps a faster speed, owing to its universal operation (rather than traversal calculation of each point).

*3) Solar Potential Evaluation:* Fig. 14 shows sunlight duration mapping using our method on the scene of Data I. The result in a top view is shown in the bottom left corner of the figure. It should be noted that our computed sunlight duration of one scene is in hours from 6:00 to 18:00 of the local time. The time when solar elevation angle is above the ground level of the rooftop but outside our computed time span does not add to accumulation of the sunlight duration. The color transition from blue to red indicates sunlight duration values varying from 0 to the maximum. In Fig. 14, to illustrate daylighting estimation and predictive capability of our method, the sunlight duration in hours is mapped for four seasons and a full year, in 2017, respectively. The four seasons begin in spring equinox (March 20), summer solstice (June 21), autumn equinox (September 23), and winter solstice (December 22), respectively. In particular, there are two periods in the winter shown in Fig. 14(e) and (f), which are from January 1 to March 19 and from December 22 to December 31.

For a single point, the annual maximum of sunlight duration is 3289 h on the rooftop handrail, averaging 9.01 h/day. This point experiences radiation from front and back during all year. The bottom left corner of the rooftop receives longer periods of illumination in spring and summer, because the sun rises over the building facade to the upper right. In autumn and winter, sunlight obliquely radiates the rooftop all day long; thus, the right side of the rooftop that is occluded by the lateral handrail becomes a nonsunlit area. As shown in Fig. 14, our results in each time period represent natural transitions in spatial distribution of the accumulation value, which demonstrates that our method works well in various moments.

Fig. 15 shows the global solar radiation calculation in Data I. Fig. 15(a)–(e) and (f)–(j) are the global solar irradiation results without and with considering a slope factor, respectively. As shown, under a clear sky index, the roof reaches a maximum value of 1940 kWh/m$^2$ without tilt correction and 1751 kWh/m$^2$ with tilt correction. In spring and summer, the sunlight irradiates roof vertically, leading to little changes in Fig. 15(b) and (g) and (c) and (h). In fall and winter, due to the oblique incidence of sunshine, the irradiation value of the rooftop main plane drops significantly under the tilt correction. On the basis of the texture of solar irradiation distribution, we can easily find the relative position of the sun and the scene in each period, which, however, will not be discussed in detail since we focus on the use of point clouds. Due to the accumulation of false points, a small number of points with incorrect irradiation values result in insufficiently smooth viewing on the distribution map. However, since those false points appear in a discrete distribution, they should not influence our results.

Table II shows the running time of annual solar potential evaluation on each item. The experimental data (Data I) after sampling contain 0.32 million points. As seen, the total time of sunlight duration and irradiation calculation with and without the tilt correction are 90.71, 91.16, and 91.50 min, respectively.

TABLE II
RUNNING TIME OF ANNUAL SOLAR POTENTIAL EVALUATION (MIN)

| Items | ROI extraction | Deviation control | Potential estimation |
|---|---|---|---|
| Sunlight duration | 0.38 | 0.01 | 90.32 |
| Irradiation (without tilt correction) | 0.38 | 0.01 | 90.77 |
| Irradiation (with tilt correction) | 0.38 | 0.01 | 91.11 |

In particular, enhanced functionality does not increase the computing burden. Owing to the range restriction of the ROI in advance, computing normal vector of a local geometry requires less calculation. Therefore, our method can be applied to *in situ* laser scanning and processing, which can provide solar potential analysis of the survey scene to even individual private customers without need for any preparation.

## V. CONCLUSION

To more accurately analyze the solar radiation of target scenes, this paper presented a method to directly process 3-D point clouds with global coordinate value without preprocessing. Our method produces the map of sunlight duration and solar radiation distribution in arbitrary time interval. In our datasets, shadow results of average accuracy of 2.44 m demonstrate the feasibility of our method.

Our future work will focus on speeding up our processing. In fact, the computation of illumination (as well as accumulated radiation) is independent for each base point. The computation can consequently be accelerated by employing parallel computing techniques. Besides, for solar radiation computing, the vegetation factor will be further considered by using an eigenvalue-based method [51], [52], which detects tree crown points.

We hope our method can be integrated into laser scanning systems (e.g., terrestrial, mobile) as a functional module to provide a function for on-spot assessment of solar potential of scanning scenes. With the only one requirement as erecting laser scanner at place of interest, this method produces a straightforward solution for beneficiaries (e.g., solar power engineer or consumer, planter, architectural planner), which is prone to be realized in engineering.

## ACKNOWLEDGMENT

## REFERENCES

[1] S. Freitas, C. Catita, P. Redweik, and M. C. Brito, "Modelling solar potential in the urban environment: State-of-the-art review," *Renew. Sustain. Energy Rev.*, vol. 41, pp. 915–931, 2015.

[2] M. Helbich, A. Jochem, W. Mücke, and B. Höfle, "Boosting the predictive accuracy of urban hedonic house price models through airborne laser scanning," *Comput. Environ. Urban*, vol. 39, no. 2, pp. 81–92, 2013.

[3] T. Higashide, "Light interception by tomato plants (solanum lycopersicum) grown on a sloped field," *Agricultural Forest Meteorol.*, vol. 149, no. 5, pp. 756–762, 2009.

[4] A. Panagopoulos, C. Wang, D. Samaras, and N. Paragios, "Simultaneous cast shadows, illumination and geometry inference using hypergraphs," *IEEE Trans. Softw. Eng.*, vol. 35, no. 2, pp. 437–449, Feb. 2013.

[5] F. Biljecki, G. B. M. Heuvelink, H. Ledoux, and J. Stoter, "Propagation of positional error in 3D GIS: Estimation of the solar irradiation of building roofs," *Int. J. Geographical Inf. Sci.*, vol. 29, no. 12, pp. 2269–2294, 2015.

[6] E. G. Melo, M. P. Almeida, R. Zilles, and J. A. B. Grimoni, "Using a shading matrix to estimate the shading factor and the irradiation in a three-dimensional model of a receiving surface in an urban environment," *Sol. Energy*, vol. 92, pp. 15–25, 2013.

[7] P. M. Rich, W. A. Hetrick, and S. C. Saving, "Modeling topographic influences on solar radiation: A manual for the SOLARFLUX model," Los Alamos Nat. Lab., Los Alamos, NM, USA, *Rep. LA-12989-M*, 1995.

[8] T. Schulmann, M. Katurji, and P. Zawar-Reza, "Seeing through shadow: Modelling surface irradiance for topographic correction of landsat ETM+ data," *ISPRS J. Photogramm. Remote Sens.*, vol. 99, pp. 14–24, 2015.

[9] J. B. Kodysh, O. A. Omitaomu, B. L. Bhaduri, and B. S. Neish, "Methodology for estimating solar potential on multiple building rooftops for photovoltaic systems," *Sustain. Cities Soc.*, vol. 8, pp. 31–41, 2013.

[10] D. A. Jacques, J. Gooding, J. J. Giesekam, A. S. Tomlin, and R. Crook, "Methodology for the assessment of PV capacity over a city region using low-resolution LiDAR data and application to the City of Leeds (UK)," *Appl. Energy*, vol. 124, pp. 28–34, 2014.

[11] T. Gál, F. Lindberg, and J. Unger, "Computing continuous sky view factors using 3d urban raster and vector databases: Comparison and application to urban climate," *Theor. Appl. Climatol.*, vol. 95, no. 1, pp. 111–123, 2008.

[12] W. Xiao, B. Vallet, M. Brédif, and N. Paparoditis, "Street environment change detection from mobile laser scanning point clouds," *ISPRS J. Photogramm. Remote Sens.*, vol. 107, pp. 38–49, 2015.

[13] R. Qin and A. Gruen, "3D change detection at street level using mobile laser scanning point clouds and terrestrial images," *ISPRS J. Photogramm. Remote Sens.*, vol. 90, pp. 23–35, 2014.

[14] A. Verso, A. Martin, J. Amador, and J. Dominguez, "GIS-based method to evaluate the photovoltaic potential in the urban environments: The particular case of Miraflores de la Sierra," *Sol. Energy*, vol. 117, pp. 236–245, 2015.

[15] A. Golovinskiy, V. G. Kim, and T. Funkhouser, "Shape-based recognition of 3D point clouds in urban environments," in *Proc. IEEE 12th Int. Conf. Comput. Vision*, 2009, pp. 2154–2161.

[16] Y. Yu, J. Li, H. Guan, F. Jia, and C. Wang, "Learning hierarchical features for automated extraction of road markings from 3-D mobile LIDAR point clouds," *IEEE J. Sel. Topics Appl. Earth Observ. Remote Sens.*, vol. 8, no. 2, pp. 709–726, Feb. 2015.

[17] B. Yang and L. Fang, "Automated extraction of 3-D railway tracks from mobile laser scanning point clouds," *IEEE J. Sel. Topics Appl. Earth Observ. Remote Sens.*, vol. 7, no. 12, pp. 4750–4761, Dec. 2014.

[18] S. R. Bucheli, Z. Pan, C. L. Glennie, A. M. Lynne, D. P. Haarman, and J. M. Hill, "Terrestrial laser scanning to model sunlight irradiance on cadavers under conditions of natural decomposition," *Int. J. Legal Med.*, vol. 128, no. 4, pp. 725–732, 2014.

[19] A. Jochem, B. Höfle, and M. Rutzinger, "Extraction of vertical walls from mobile laser scanning data for solar potential assessment," *Remote Sens.*, vol. 3, no. 4, pp. 650–667, 2011.

[20] F. Lindberg, P. Jonsson, T. Honjo, and D. Wästberg, "Solar energy on building envelopes—3D modelling in a 2D environment," *Sol. Energy*, vol. 115, pp. 369–378, 2015.

[21] T. Santos, N. Gomes, S. Freire, M.C. Brito, L. Santos, and J. A. Tenedorio, "Applications of solar mapping in the urban environment," *Appl. Geography*, vol. 51, pp. 48–57, 2014.

[22] H. T. Nguyen and J. M. Pearce, "Incorporating shading losses in solar photovoltaic potential assessment at the municipal scale," *Sol. Energy*, vol. 86, no. 5, pp. 1245–1260, 2012.

[23] B. Yu, H. Liu, J. Wu, and W. M. Lin, "Investigating impacts of urban morphology on spatio-temporal variations of solar radiation with airborne LiDAR data and a solar flux model: A case study of downtown Houston," *Int. J. Remote Sens.*, vol. 30, no. 17, pp. 4359–4385, 2009.

[24] A. Strzalka, N. Alam, E. Duminil, V. Coors, and U. Eicker, "Large scale integration of photovoltaics in cities," *Appl. Energy*, vol. 93, pp. 413–421, 2012.

[25] N. A. Akel, S. Filin, and Y. Doytsher, "Reconstruction of complex shape buildings from lidar data using free form surfaces," *Photogramm. Eng. Remote Sens.*, vol. 75, no. 3, pp. 271–280, 2009.

[26] C. Catita, P. Redweik, J. Pereira, and M. C. Brito, "Extending solar potential analysis in buildings to vertical facades," *Comput. Geosci.*, vol. 66, pp. 1–12, 2014.

[27] G. Gröger and L. Plümer, "CityGML—Interoperable semantic 3D city models," *ISPRS J. Photogramm. Remote Sens.*, vol. 71, pp. 12–33, 2012.

[28] F. Biljecki, H. Ledoux, J. Stoter, and G. Vosselman, "The variants of an LOD of a 3D building model and their influence on spatial analyses," *ISPRS J. Photogramm. Remote Sens.*, vol. 116, pp. 42–54, 2016.

[29] A. Kato, L. M. Moskal, P. Schiess, M. E. Swansonc, D. Calhound, and W. Stuetzlee, "Capturing tree crown formation through implicit surface reconstruction using airborne lidar data," *Remote Sens. Environ.*, vol. 113, no. 6, pp. 1148–1162, 2009.

[30] F. Biljecki, H. Ledoux, and J. Stoter, "Does a finer level of detail of a 3D city model bring an improvement for estimating shadows?" in *Advances in 3D Geoinformation*. Berlin, Germany: Springer, 2017.

[31] A. Jochem, B. Höfle, M. Rutzinger, and N. Pfeifer, "Automatic roof plane detection and analysis in airborne lidar point clouds for solar potential assessment," *Sensors*, vol. 9, no. 7, pp. 5241–5262, 2009.

[32] N. Lukač, D. Žlaus, S. Seme, B. Žalik, and G. Štumberger, "Rating of roofs' surfaces regarding their solar potential and suitability for PV systems, based on LiDAR data," *Appl. Energy*, vol. 102, pp. 803–812, 2013.

[33] N. Lukač, and B. Žalik, "GPU-based roofs' solar potential estimation using LiDAR data," *Comput. Geosci.*, vol. 52, pp. 34–41, 2013.

[34] N. Lukač, S. Seme, D. Žlaus, G. Štumberger, and B. Žalik, "Buildings roofs photovoltaic potential assessment based on LiDAR (Light Detection And Ranging) data," *Energy*, vol. 66, pp. 598–609, 2014.

[35] P. Redweik, C. Catita, and M. C. Brito, "PV potential estimation using 3D local scale solar radiation model based on urban LIDAR data," in *Proc. the 26th Eur. Photovoltaic Solar Energy Conf.*, Hamburg, Germany, 2011, pp. 3–5.

[36] Y. Yu, J. Li, H. Guan, C. Wang, and J. Yu, "Semiautomated extraction of street light poles from mobile LiDAR point-clouds," *IEEE Trans. Geosci. Remote Sens.*, vol. 53, no. 3, pp. 1374–1386, Mar. 2015.

[37] Y. Yu, J. Li, H. Guan, and C. Wang, "Automated detection of three-dimensional cars in mobile laser scanning point clouds using DBM-Hough-Forests," *IEEE Trans. Geosci. Remote Sens.*, vol. 54, no. 7, pp. 4130–4142, Jul. 2016.

[38] R. Grena, "An algorithm for the computation of the solar position," *Sol. Energy*, vol. 82, no. 5, pp. 462–470, 2008.

[39] P. I. Cooper, "The absorption of radiation in solar stills," *Sol. Energy*, vol. 12, no. 3, pp. 333–346, 1969.

[40] S. Katz and A. Tal, "On the visibility of point clouds," in *Proc. IEEE Int. Conf. Comput. Vision*, 2015, pp. 1350–1358.

[41] Y. Eldar, M. Lindenbaum, M. Porat, and Y. Y. Zeevi, "The farthest point strategy for progressive image sampling," *IEEE Trans. Image Process.*, vol. 6, no. 9, pp. 1305–1315, Sep. 1997.

[42] C. Moenning and N. A. Dodgson, "A new point cloud simplification algorithm," in *Proc. 3rd IASTED Conf. Vis., Imag. Image Process.*, 2003, pp. 1027–1033.

[43] S. Katz and A. Tal, "Improving the visual comprehension of point sets," in *Proc. IEEE Conf. Comput. Vision Pattern Recognit.*, 2013, pp. 121–128.

[44] E. Shtrom, G. Leifman, and A. Tal, "Saliency detection in large point sets," in *Proc. IEEE Int. Conf. Comput. Vision*, 2013, pp. 3591–3598.

[45] S. Katz, A. Tal, and R. Basri, "Direct visibility of point sets," *ACM Trans Graph.*, vol. 26, no. 3, 2007, Art. no. 24.

[46] H. D. Cheung, and T. M. Chung, "Analyzing sunlight duration and optimum shading using a sky map," *Build. Environ.*, vol. 42, no. 9, pp. 3138–3148, 2007.

[47] P. Littlefair, "Daylight, sunlight and solar gain in the urban environment," *Sol. Energy*, vol. 70, no. 3, pp. 177–185, 2001.

[48] L. Kumar, A. K. Skidmore, and E. Knowles, "Modelling topographic variation in solar radiation in a GIS environment," *Int. J. Geographical Inf. Sci.*, vol. 11, no. 5, pp. 475–497, 1997.

[49] H. C. Hottel, "A simple model for estimating the transmittance of direct solar radiation through clear atmospheres," *Sol. Energy*, vol. 18, no. 2, pp. 129–134, 1976.

[50] A. Jochem, B. Höfle, M. Hollaus, and M. Rutzinger, "Object detection in airborne LIDAR data for improved solar radiation modeling in urban areas," *Int. Arch. Photogrammetry, Remote Sens. Spatial Inf. Sci.*, vol. 38, pp. 1–9, 2009.

[51] J. F. Lalonde, N. Vandapel, D. F. Huber, and M. Hebert, "Natural terrain classification using three-dimensional ladar data for ground robot mobility," *J. Field Robot.*, vol. 23, no. 10, pp. 839–862, 2006.

[52] B. Yang and Z. Dong. "A shape-based segmentation method for mobile laser scanning point clouds," *ISPRS J. Photogramm. Remote Sens.*, vol. 81, pp. 19–30, 2013.

**Pengdi Huang** received the M.Sc. degree in optical engineering from Yunnan Normal University, Kunming, China, in 2013. He is currently working toward the Ph.D. degree in information and communication engineering with the Fujian Key Laboratory of Sensing and Computing for Smart Cities and the Department of Communication Engineering, School of Information Science and Engineering, Xiamen University, Xiamen, China.

His current research interests include computer vision, 3-D point cloud processing, object detection and extraction, and mobile laser scanning data processing.



**Ming Cheng** (M'14) received the Ph.D. degree in biomedical engineering from Tsinghua University, Beijing, China, in 2004.

He is currently an Associate Professor with the Fujian Key Laboratory of Sensing and Computing for Smart Cities and the Xiamen Key Laboratory of Geospatial Sensing and Computing, School of Information Science and Engineering, Xiamen University, Xiamen, China. His research interests include remote sensing image processing, point cloud processing, computer vision, and machine learning. He has published more than 30 papers in refereed journals and conference proceedings, including the IEEE GEOSCIENCE AND REMOTE SENSING LETTERS, *Neurocomputing*, and *IGARSS and ISPRS proceedings*.



**Yiping Chen** received the Ph.D. degree in information and communication engineering from the National University of Defense Technology, Changsha, China, in 2011.

She is an Assistant Professor at the National University of Defense Technology and a Postdoctoral Fellow with the Fujian Key Laboratory of Sensing and Computing for Smart Cities, School of Information Science and Engineering, Xiamen University, Xiamen, China. She was as a Research Assistant at the Chinese University of Hong Kong from 2007 to 2011. Her current research interests include image processing, mobile laser scanning data analysis, and automated detection of 3-D objects in point clouds.



**Dawei Zai** received the B.Sc. degree in aircraft design and engineering from Xi'an Jiaotong University, Xi'an, China, in 2010. He is currently working toward the Ph.D. degree in information and communication engineering with the Fujian Key Laboratory of Sensing and Computing for Smart Cities, Xiamen University, Xiamen, China.

His current research interests include computer vision, machine learning, and mobile laser scanning point cloud data processing.

**Cheng Wang** (M'04–SM'16) received the Ph.D. degree in information and communication engineering from the National University of Defense Technology, Changsha, China, in 2002.

He is a Professor with the Fujian Key Laboratory of Sensing and Computing for Smart Cities and an Associate Dean of the School of Information Science and Technology, Xiamen University, Xiamen, China. His current research interests include remote sensing image processing, mobile LiDAR data analysis, and multisensor fusion. He has coauthored about 150 papers published in refereed journals such as the IEEE TRANSACTIONS ON GEOSCIENCE AND REMOTE SENSING, IEEE TRANSACTIONS ON INTELLIGENT TRANSPORTATION SYSTEMS, IEEE GEOSCIENCE AND REMOTE SENSING LETTERS, IEEE JOURNAL OF SELECTED TOPICS IN APPLIED EARTH OBSERVATIONS AND REMOTE SENSING, and *ISPRS Journal of Photogrammetry and Remote Sensing* and conferences such as IGARSS and ISPRS.

Dr. Wang is the Chair of the ISPRS Working Group I/6 on Multisensor Integration and Fusion (2016–2020). He is a Council Member of the Chinese Society of Image and Graphics.

**Jonathan Li** (M'00–SM'11) received the Ph.D. degree in geomatics engineering from the University of Cape Town, Cape Town, South Africa, in 2000.

He is a Professor with the Fujian Key Laboratory of Sensing and Computing for Smart Cities and the School of Information Science and Engineering, Xiamen University, Xiamen, China. He is also a Professor and the Head of the WatMos Lab, Faculty of Environment, University of Waterloo, Waterloo, ON, Canada. His current research interests include information extraction from LiDAR point clouds and from earth observation images. He has coauthored more than 300 publications, more than 130 of which were published in refereed journals, including IEEE TRANSACTIONS ON GEOSCIENCE AND REMOTE SENSING, IEEE TRANSACTIONS ON INTELLIGENT TRANSPORTATION SYSTEMS (IEEE TITS), IEEE GEOSCIENCE AND REMOTE SENSING LETTERS, IEEE JOURNAL OF SELECTED TOPICS IN APPLIED EARTH OBSERVATIONS AND REMOTE SENSING (IEEE JSTARS), *ISPRS Journal of Photogrammetry and Remote Sensing*, *International Journal of Reliability and Safety*, *Photogrammetric Engineering and Remote Sensing*, and *Remote Sensing of Environment*.

Dr. Li is the Chair of the ISPRS Working Group I/2 on LiDAR-, Air- and Spaceborne Optical Sensing (2016–2020), the Chair of the ICA Commission on Sensor-driven Mapping (2015–2019), and an Associate Editor of IEEE-TITS and IEEE-JSTARS.